



A Compliant Transoral Surgical Robotic System Based on a Parallel Flexible Mechanism

XIAOYI GU,^{1,3} CHANGSHENG LI,¹ XIAO XIAO,¹ CHWEE MING LIM,² and HONGLIANG REN^{1,3}

¹Department of Biomedical Engineering, National University of Singapore, EA-05-30, 9 Engineering Drive 1, Singapore 117575, Singapore; ²Department of Otolaryngology-Head and Neck Surgery, National University Hospital, Singapore, Singapore; and ³National University of Singapore (Suzhou) Research Institute, Suzhou, China

(Received 12 November 2018; accepted 1 March 2019; published online 12 March 2019)

Associate Editor Ka-Wai Kwok oversaw the review of this article.

Abstract—Transoral robotic surgery (TORS) allows for access to oropharyngeal regions in an effective and minimally invasive manner. However, safe TORS access to deep pharyngeal (such as hypopharynx) sites remains a great challenge for current surgical robotic systems. In this work, we introduce a novel continuum robot with an optimized flexible parallel mechanism, to meet stringent requirements imposed by TORS on size, workspace, flexibility, and compliance. The system is comprised of two parts, a guidance part and an execution part, and achieves 11 controllable degrees of freedom. The execution part of the robot, based on the optimized flexible parallel mechanism, is able to reach deep sites in the oropharynx and larynx with the assistance of the continuum guidance part. In addition to the mechanical design, extensive analysis and experiments were carried out. Kinematic models were derived and the reachable workspace of the robot was verified to cover the entire target surgical area. Experimental results indicate that the robot achieves significantly enhanced compliance. Additionally, the designed robot can withstand a load of 1.5 N within the allowable range of the deflection. The positioning errors caused by the interference between different mechanisms can be effectively eliminated using the proposed compensation method. The maximum displacement error of this system under various conditions is less than 2 mm and the maximum bending error is less than 7.5°, which are satisfied for TORS. Cadaver trials were conducted to further demonstrate the feasibility. The reduced setup time and the reduced time to access the target site indicate that the developed surgical robotic system can achieve better operative efficiency in TORS when compared with current systems.

Keywords—TORS, Surgical robot, Hybrid mechanism, Continuum robot, Flexible parallel robot.

INTRODUCTION

The upper aerodigestive tract, including the oropharynx and larynx, has a long, narrow, and irregularly arc-shaped operative space, leading to great difficulties in the treatment of diseases in these areas.¹⁹ As a typical form of minimally invasive surgery (MIS), transoral surgery (TOS) gains access to the surgical site through the oral cavity. Therefore, TOS offer patients alternatives to conventional open approaches with minimized trauma, shortened hospital time, improved outcome, and obvious cosmetic improvements. However, the development of TOS is facing a bottleneck due to the use of traditional surgical instruments. The insufficient distal dexterity of these instruments and the fulcrum effect caused by the insertion port result in the loss of direct hand–eye coordination and motion scaling.¹⁹ Additionally, the use of the suspension laryngoscope incurs a high risk of inducing a variety of complications.²⁵

Robotic technology is capable of restoring and augmenting the reduced perception and motor skills of surgeons in the confined intra-body environment,^{2,5} which makes it possible to address challenges and realize the full potential of TOS.¹¹ This emerging procedure is termed transoral robotic surgery (TORS). To the best of our knowledge, two surgical robotic systems have obtained FDA approval to be marketed for TORS. The Da Vinci® robotic system (Intuitive Surgical, Inc., CA, USA) is a widely used surgical robotic system in TORS. Although the system has achieved encouraging oncological and functional outcomes,²⁰ bulky operating forearms and a rigid straight configuration make operation in tight cavities challenging. Moreover, the workspace of this surgical robotic system is constrained to the oropharynx,

Address correspondence to Hongliang Ren, Department of Biomedical Engineering, National University of Singapore, EA-05-30, 9 Engineering Drive 1, Singapore 117575, Singapore. Electronic mails: hlren@iee.org, ren@nus.edu.sg

restricting its applications in deeper anatomical sites.²² The Flex[®] surgical system (Medrobotics, Inc., Raynham, MA, USA) has increased flexibility and a larger workspace. Nevertheless, the lack of the master–slave control system, slow motion, and limited load capability deteriorate its performance in TORS.^{16,22}

Technically, surgical robotic systems with various mechanisms have been developed for MIS.^{2,4,30,31} Most surgical robots adopt the serial mechanism, which is composed of discrete and rigid links.^{9,10,21} Because every joint is independently controllable, this type of robot features a relatively large workspace and achieves high dexterity as well as high motion accuracy. Nevertheless, the incapacity of rigid links to bend continuously leads to decreased compliance.²⁴ Scaling down the size while retaining reliability is another difficulty that precludes the utilization of such robots in TORS. Parallel mechanisms, which are characterized by high precision, enhanced load capacity, increased dexterity, and excellent reliability, have also been employed in the design of surgical robots.^{12,23,27} In addition to minimizing of the size, their extremely high stiffness and low compliance will lead to serious safety issues.⁸ Compared with these two mechanisms, the continuum robot is more suitable for medical application due to its inherent structural compliance and ease of miniaturization, compared with rigid multi-body kinematics.^{4,32} However, complicated modelling analysis results in decreased motion accuracy. In addition, the workspace and load capacity are reduced compared with fully actuated robots.¹⁷

Efforts have been made to investigate new design concepts that integrate multiple mechanisms, termed hybrid mechanisms. The serial robot and the continuum robot are combined in the design of a multitasking surgical robot,²⁸ which contributes to improved flexibility and a larger workspace. A similar design concept involving the insertion of rigid joints between continuum segments achieved better security than did serial robots and more precise motion control than did continuum robots.⁶ Recently, a bending mechanism, referred to as the parallel continuum mechanism, was shown able to retain advantages of both the rigid-link parallel robot and the continuum robot.³ As shown in Table 1, a single mechanism has its own merits and demerits and cannot satisfy all the requirements of TORS. In contrast, hybrid mechanisms, which inherit advantages from every single mechanism and remedy their shortcomings by drawing the strengths of others, are able to achieve comprehensively improved performance compared to single mechanisms. Therefore, a suitable hybrid mechanism is believed to have the ability to meet the strict requirements imposed by TORS.

In this work, a novel hybrid mechanism is proposed and employed in developing a surgical robotic system

for TORS. The major contributions of this work can be captured by the following four aspects: To the best of the authors' knowledge, this is the first attempt to connect the design concept of a continuum robot and the flexible parallel mechanism in the development of a surgical robot. Additionally, the flexible parallel mechanism is optimized based on our previous design,¹⁵ which has a simplified structure for alleviating the interference between different mechanisms. Furthermore, kinematic analysis and extensive investigations, including bending stiffness characterization, positioning accuracy testing, and load capability evaluation were carried out to evaluate the performance of the developed surgical robotic system. Finally, cadaver trails were successfully implemented in a master–slave teleoperation mode, demonstrating the feasibility and efficiency of the designed surgical robotic system in TORS.

MATERIALS AND METHODS

Design Goals

To pass through the oral cavity and conduct surgical interventions in the complex and confined environments of the oropharynx and larynx, five design goals should be achieved in the development of a robot for TORS. First, the cross-section of the distal part of the robot should be within a circle with a diameter of 20 mm.²⁶ Second, the robot should have the ability to generate a bending motion with a maximum angle larger than 90° to bypass the epiglottis. Third, the reachable workspace of the robot should have a volume larger than 30 mm * 25 mm * 50 mm to cover the whole space of target surgical areas.^{7,26} Fourth, the robot is expected to have a reasonable bending stiffness to obtain adequate compliance and protect crucial tissues. Finally, the robot should achieve quick installation and shortened setup time during a surgery.

Robot Design

Figure 1 provides an overview of the surgical robotic system developed in this work for TORS, which consists of an execution part and a guidance part (see Fig. 1c). During a typical TORS procedure, the execution part, which contains two manipulators and one vision unit, is facilitated by the guidance part to reach the target surgical site by traversing the oral cavity as shown in Fig. 1b. The flexible parallel mechanism, based on which two manipulators and a vision unit are developed, is optimized to improve performance and be combined with the bendable segment, which adopts the design concept of a continuum robot to constitute

TABLE 1. Features of surgical robots with different mechanisms.

	Serial robots	Continuum robots	Parallel robots	Hybrid mechanisms
Workspace	+++++	+++	+	+++++
Flexibility	+	+++++	+	+++++
Dexterity	+++	+	+++++	+++++
Compliance	+	+++++	+	+++++
Load capacity	+++++	+	+++++	+++
Accuracy	+++++	+	+++++	+++++
Scaling down	+	+++++	+	+++

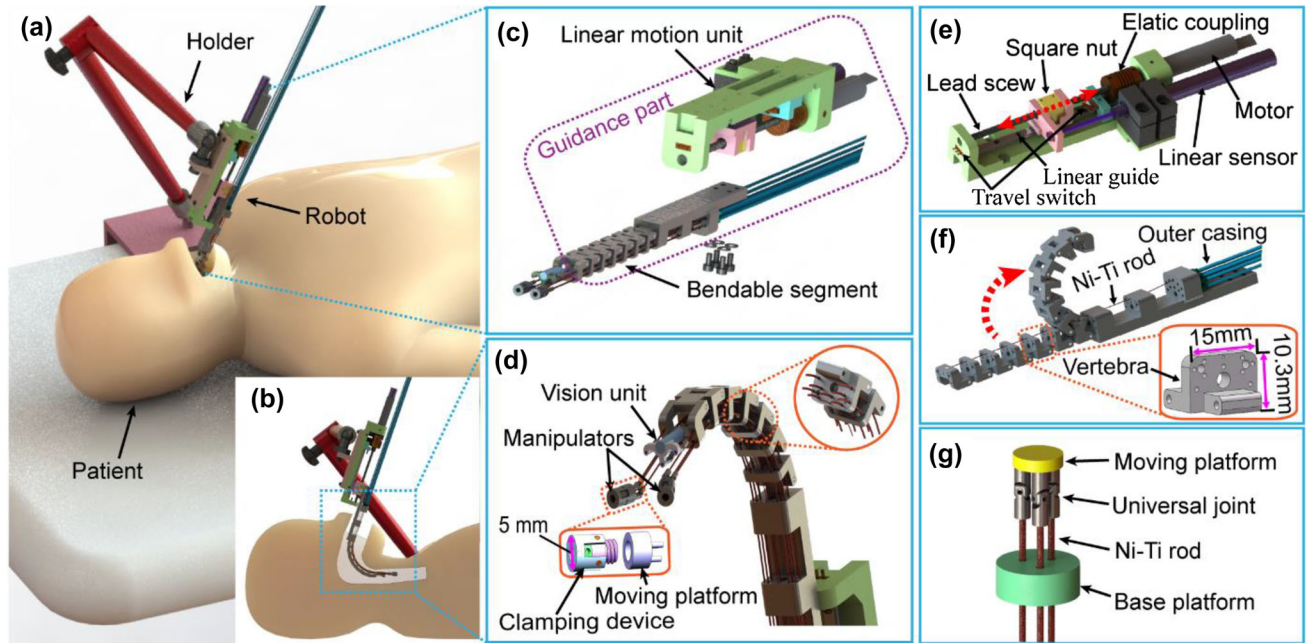


FIGURE 1. Overview of the designed surgical robotic system: (a) surgical scenario. (b) Section view of the robot in the working state. (c) Exploded diagram of the guidance part. (d) Execution part. (e) Linear motion unit. (f) Bendable segment. (g) Optimized flexible parallel mechanism.

a novel hybrid mechanism. Owing to the nickel–titanium (Ni–Ti) rod based actuation mechanism, the actuation part is separated from the main body of the robot, which further reduces the size of the robot. Consequently, the designed robot has a compact structure of $200 \text{ mm} \times 50 \text{ mm} \times 46.5 \text{ mm}$ and a light weight of 480 g, which can be easily attached to a multi-degrees of freedom (multi-DOF) stand mounted to a hospital bed, as depicted in Fig. 1a, satisfying the compatibility requirement of most operating theatres.³⁰

The execution part is responsible for completing surgical operations and providing visual feedback to the operator. As illustrated in Fig. 1d, the vision unit is located above two manipulators, which enables more intuitive control of the manipulators. Both the manipulator and the vision unit are developed based on a flexible 3-PU parallel mechanism. In our previous

work,¹⁵ superelastic Ni–Ti rods were utilized to replace part of the rigid links of a conventional parallel robot, which was verified to provide significant improvements to the robot in terms of compact structure and better flexibility. This flexible parallel mechanism was further optimized in this work such that both the manipulator and the vision unit can be combined with the guidance part. As depicted in Fig. 1g, each serial chain was simply composed of a universal (U) joint and a Ni–Ti rod (diameter 0.6 mm). One end of a universal joint is fixed to the moving platform and the other end is connected to a Ni–Ti rod. A Ni–Ti rod passing through a hole in the base platform forms a prismatic (P) joint, which is directly connected to the actuation part. Taking advantage of the flexible deformation of Ni–Ti rods, this optimized 3-PU flexible parallel mechanism can still achieve 3-DOF motions, including 2-DOF bending motions and one linear motion, by

pushing/pulling three Ni–Ti rods. Compared with our previous design and other studies employing Ni–Ti rods, the distinctions and superiorities of this mechanism are embodied in the following four aspects: First, rigid links are completely removed and replaced by slender and super-elastic Ni–Ti rods, which contributes to a more compact structure, simpler assembly process, and reduced manufacturing cost. Second, the Ni–Ti rod-based actuation method plays a similar role as the cable-driven mechanism in reducing the size of the robot. Moreover, errors caused by intermediate transmission components, e.g., flexible shaft,¹⁵ can be eliminated. Third, in addition to two dexterous and flexible manipulators, the vision unit possesses three independently controllable DOFs, which are able to provide the operator with a wider and more flexible angle of view. Finally, the minimal bending radius of this mechanism is 4.22 mm while other designs employing Ni–Ti rods have a bending radius larger than 5 mm,^{13,19} which contributes to the better dexterity of this robot.

To quickly replace surgical instruments during surgery, a detachable clamping device with a diameter of 5 mm was carefully designed, which is connected to the moving platform by screw threads, as depicted in Fig. 1d.

The guidance part, which is composed of a linear motion unit and a bendable segment, was designed to facilitate the execution part in reaching the target surgical site. Figure 1e shows the CAD model of the linear motion unit. The output shaft of a motor (RE 13, Maxon Motor, Inc., Sachseln, Switzerland) is connected to a lead screw (diameter 4 mm, lead 1 mm) *via* an elastic coupling. A square nut is matched with the lead screw and fixed to the slide block of a linear guide. Thus, the square nut has only one controllable translational DOF with a maximum displacement equal to 80 mm. To enhance the safety of the robot, micro limit switches are utilized to avoid the collision between the square nut and other components. Additionally, a linear displacement sensor (KP12-100, Miran Technology Co., Ltd., Shenzhen, China) is utilized to provide position information for feedback control. The bendable segment, which is bolted to the square nut of the linear motion unit (see Fig. 1c), is the part that will move in the confined and complex in-body environment and has a high probability contacting crucial tissues. For adequate flexibility and compliance, the design concept of continuum robots is employed in the design of this part. As depicted in Fig. 1f, a number of identical vertebrae are sequentially connected to form a series of revolute joints. For each vertebra, the cross-section is 15 mm × 10.3 mm, satisfying the design goal. By pulling a Ni–Ti rod (diameter 0.3 mm) with one end fixed to the distal ver-

tebra, the bendable segment can bend to a maximum angle of 180°. In addition, tubes made of Teflon, which is a type of self-lubricating material, are used as the outer casings.

In this work, the optimized flexible parallel mechanism and the continuum structure of the guidance part were skillfully combined to constitute a novel hybrid mechanism. As depicted in Fig. 1d, Ni–Ti rods, which are used to drive motions of the execution part, pass through pinholes in vertebrae with the distal vertebra serving as the base platform for the manipulators and the vision unit. Due to their superelasticity, the Ni–Ti rods of the execution part can conform to the shape of the bendable segment, in which case these Ni–Ti rods can still generate pulling/pushing movements to control the motions of the flexible parallel mechanism. The linear motion of these Ni–Ti has no influence on the bending motion of the guidance part, as confirmed by the results of the positioning accuracy tests. In this hybrid mechanism, the guidance part operates as an “arm” and the manipulator plays the role as a “wrist”. For the guidance part, the super-elastic rods provide the indispensable elasticity of the continuum structure, which contributes to the robot’s enhanced compliance and safer interactions with patient tissues of the robot. Meanwhile, the maximum linear displacement of the manipulator is increased from 20 to 120 mm and the maximum bending angle is up to 225°. The total number of controllable DOFs of the robot is 11. Consequently, this hybrid mechanism contributes to the compact structure, enhanced compliance, improved flexibility, and increased workspace of the robot. Although the bending motion of the guidance part will lead to the distortion of the manipulator and the vision unit, this problem can be alleviated by keeping the orientation of the manipulator and the vision unit relative to the distal vertebra of the bendable segment unchanged. This compensation method is also of great importance for enhancing the maneuverability of the manipulator. Additionally, the bending motion of the bendable segment has no influence on the DOF or the motion range of the execution part. The impact caused by the bending motion on the positioning accuracy of the manipulator was investigated as described in the experimental part.

Figure 2 shows the actuation part of the surgical robotic system, which contains four controller boards (SIMLAB, Zeltom Co., Ltd., Michigan, USA), nine identical small linear actuation units for the control of the execution part, and one large linear actuation unit for the actuation of the bending motion of the guidance part. The bending motion of the guidance part requires a relatively large actuation force. As a result, a higher-power motor (RE25, Maxon Motor, Inc., Sachseln, Switzerland) is utilized in the large linear

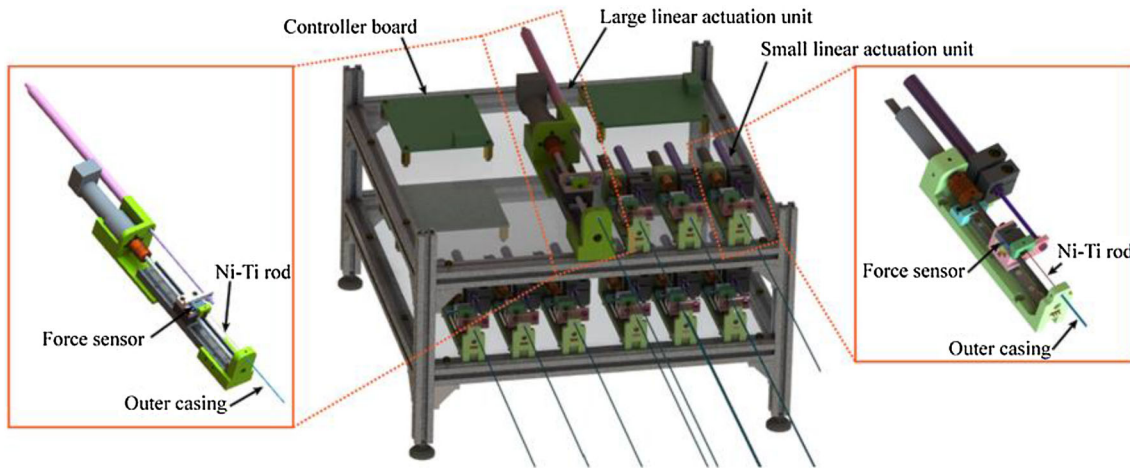


FIGURE 2. CAD model of the actuation part.

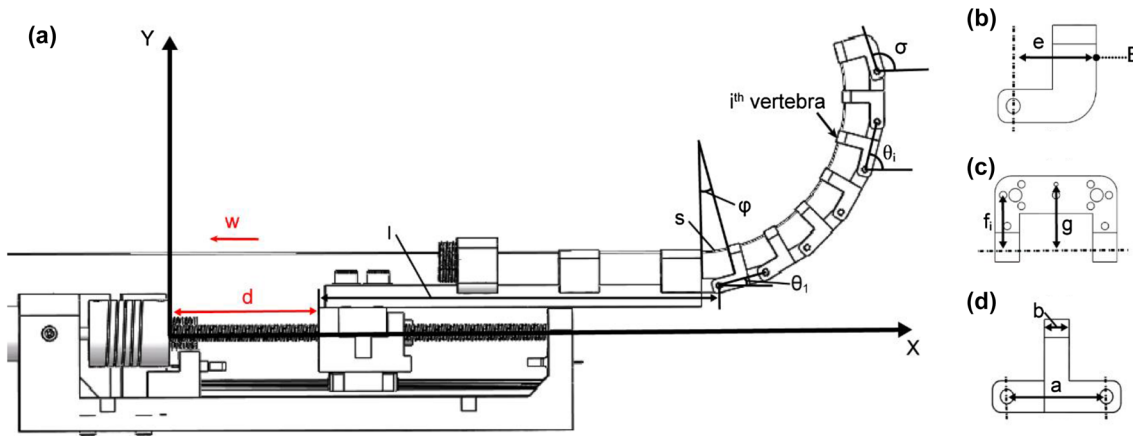


FIGURE 3. Parameters for kinematic analysis. (a) Parameters of the guidance part. (b) Parameters of the side view of the distal vertebra. (c) Parameters of the front view of the distal vertebra. (d) Parameters of the side view of the i th vertebra.

actuation unit. The small linear actuation unit adopts the same motor as the linear motion unit. As illustrated in Fig. 2, both linear motion units have a structure similar to the linear motion unit and operate according to the same principle. There are two major modifications. First, the outer casing of Ni–Ti rods is fixed to the base using set screws, which can be easily removed and replaced. Second, the Ni–Ti rod is connected to the square nut *via* a force sensor. Thus, the actuation force on the Ni–Ti rod can be measured.

Kinematic Analysis

The parameters of the guidance part are described in a plane as shown in Fig. 3a. The coordinate frame O-XY is attached to the center of the elastic coupling with the X-axis coinciding with the center-line of the lead screw. x is the position of point E on the X-axis,

which denotes the insertion depth of the guidance part. The angle σ between the distal vertebra and the X-axis is referred to as the bending angle of the guidance part. According to the geometrical relationship, the insertion depth x can be expressed as follows:

$$x = d + l + a(\cos \theta_1 + \cos \theta_2 + \dots + \cos \theta_{n-1}) + e \cos \sigma, \tag{1}$$

where d is the displacement of the slide block of the linear motion unit, l , a and b are geometric parameters, n is the number of the vertebra, and θ_i is the bending angle between the i th vertebra and the X-axis. In the absence of an external load, the bending angles between adjacent vertebrae are assumed to be identical. Consequently, θ_i can be expressed as follows:

$$\theta_i = \frac{\sigma}{n} \times i \quad (i = 1, 2, \dots, n - 1). \tag{2}$$

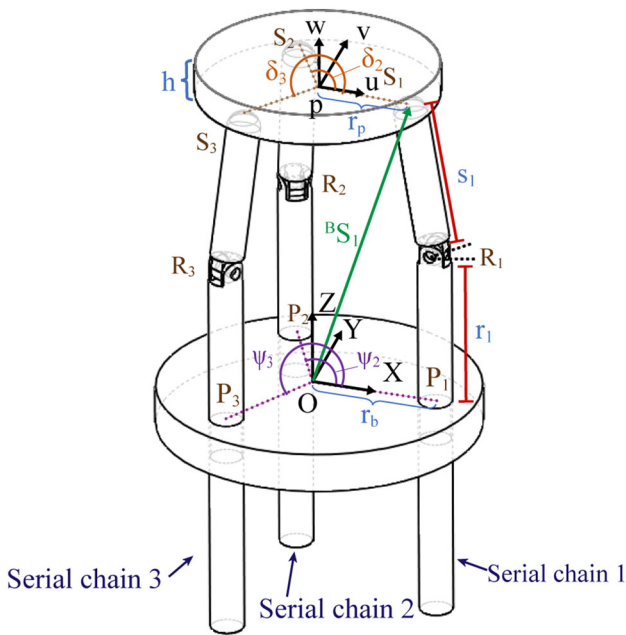


FIGURE 4. Parameters for kinematic analysis of the optimized flexible parallel mechanism.

Substituting Eq. (2) into (1) yields:

$$d = \left(x - l + \frac{a}{2}\right) + \left(\frac{a}{2} - e\right) \times \cos \sigma - \frac{a}{2} \sin \sigma \cot \frac{\sigma}{12}. \tag{3}$$

The bending angle of the guidance part is determined by the displacement of the Ni–Ti rod utilized to control the bending motion. The displacement of this Ni–Ti rod w can be written as follows:

$$w = n \times \Delta s = n \times \left((a - b) - \left(\frac{a - b}{2 \tan(\frac{\sigma}{2n})} - g \right) \times \varphi \right), \tag{4}$$

where Δs is the variation in a single arc length, φ is the degree of curvature of a single arc, and b and g are geometric parameters of a vertebra. Geometrically, φ equals θ_1 . Therefore, Eq. (4) can be represented as follows:

$$w = n \times \left((a - b) - \left(\frac{a - b}{2 \tan(\frac{\sigma}{2n})} - g \right) \times \frac{\sigma}{n} \right) \quad (\sigma \neq 0). \tag{5}$$

When σ equals 0, the bendable segment is at its initial state, in which case the displacement of the Ni–Ti rod remains 0. Hence, if x and σ are given, d and w can be obtained using Eqs. (3) and (5).

To implement the proposed compensation method, Ni–Ti rods are required to shift by corresponding distances according to the bending angle of the bendable segment. For j th Ni–Ti rod, the displacement c_j can be written as follows:

$$c_j = n \times \left((a - b) - \left(\frac{a - b}{2 \tan(\frac{\sigma}{2n})} - f_j \right) \times \frac{\sigma}{n} \right) \quad (\sigma \neq 0), \tag{6}$$

where f_j is the distance between the center of the hole passed through by j th Ni–Ti rod and the rotation axis of the vertebra.

In our previous work,¹⁵ the Ni–Ti rod based flexible parallel mechanism was simplified as a 3-PRS mechanism for the kinematic analysis, which was verified to be effective to describe the relationship between the motion of the moving platform and displacements of three Ni–Ti rods. The derived kinematic model was utilized in this work for the workspace analysis and control of the designed manipulator, the effectiveness of which was investigated as described in the experiment part.

As illustrated in Fig. 4, two coordination frames $O-XYZ$ and $p-uvw$ are attached to the center of the base platform and moving platforms, respectively. Three serial chains of the mechanism are marked by k ($k = 1, 2, 3$). In serial chain k , P_k is the intersection between the center line of the prismatic joint and the XY plane, R_k denotes the center of the revolute joint, and S_k represents the center of the spherical joint. The X -axis of $O-XYZ$ is coincident with the vector P_1 . The u -axis of $p-uvw$ is aligned to the vector S_1 . ${}^B P_k$ is the position vector of P_k expressed in the base coordinate frame $O-XYZ$, which can be expressed as follows:

$${}^B P_k = [P_{kX} \ P_{kY} \ P_{kZ}] = [r_b \cos \varphi_k \ r_b \sin \varphi_k \ 0], \tag{7}$$

where r_b is the length of P_k , and φ_k is the angle between P_k and the X -axis.

Similarly, the position vector of S_k can be expressed in the moving coordinate frame $p-uvw$ as follows:

$${}^P S_k = [S_{ku} \ S_{kv} \ S_{kw}] = [r_p \cos \delta_k \ r_p \sin \delta_k \ 0] \tag{8}$$

here r_p is the length of S_k , and δ_k is the angle between k and the u -axis.

T is the center of the distal end of the moving platform, whose position vector in the base platform coordinate and in the moving platform coordinate can be expressed respectively as:

$${}^P T = [00h]^T, \tag{9}$$

TABLE 2. Configuration parameters of the guidance part.

Parameters	Values	Units	Parameters	Values	Units
n	6		a	12.00	mm
l	98.50	mm	b	3.00	mm
d_{\max}	80.00	mm	e	9.50	mm
σ_{\max}	180.00	°	g	8.05	mm

TABLE 3. Configuration parameters of the manipulator.

Parameters	Values	Units	Parameters	Values	Units
r_b	1.50	mm	δ_k	$120(i-1)$	°
r_p	1.50	mm	s_k	3.50	mm
φ_k	$120(i-1)$	°	h	20.00	mm
α_{\max}	45.00	°	r_{\max}	20.00	mm
β_{\max}	45.00	°			

$${}^B T = {}^B p + R^P T = [T_X \ T_Y \ T_Z]^T, \quad (10)$$

where h is the thickness of the moving platform, ${}^B p$ is the position vector of P expressed in the base coordinate frame, which can be expressed as follows:

$${}^B p = [p_X \ p_Y \ p_Z]^T. \quad (11)$$

R is the rotation matrix represented by the Euler angles (the first rotation of γ about the Z -axis, followed by the second rotation of α about the X -axis, and the third rotation of β about the Y -axis), which can be expressed as follows:

$$R = R_Y(\beta)R_X(\alpha)R_Z(\gamma) = \begin{bmatrix} c\beta c\gamma + s\alpha s\beta c\gamma & -c\beta s\gamma + s\alpha s\beta s\gamma & c\alpha s\beta \\ c\alpha s\gamma & c\alpha c\gamma & -s\alpha \\ -s\beta c\gamma + s\alpha c\beta c\gamma & s\alpha s\gamma + s\alpha c\beta s\gamma & c\alpha c\beta \end{bmatrix}, \quad (12)$$

where c represents \cos , and s represents for \sin .

For the inverse kinematic analysis, the following vector-loop equations can be obtained from the geometry of serial chains:

$${}^B S_k = [S_{kX} \ S_{kY} \ S_{kZ}]^T = {}^B p + R^P S_k, \quad (13)$$

where ${}^B S_k$ is the position vector of S_k in the base coordinate frame.

Mechanical constraints imposed by revolute joints allow S_k to move only in the plane defined by O , P_k , R_k , and S_k . As a result, the following equations can be derived:

$$\tan \varphi_i = \frac{S_{iX}}{S_{iY}}. \quad (14)$$

Substituting Eqs. (7)–(12), and (14) into (13) yields:

$$\begin{cases} p_X = \frac{r_p}{2} (c\beta c\gamma + s\alpha s\beta s\gamma - c\alpha c\gamma), \\ p_Y = -r_p c\alpha s\gamma, \\ p_Z = T_Z - hc\alpha c, \\ \gamma = \tan^{-1} \frac{s\alpha s\beta}{c\alpha + c\beta}. \end{cases} \quad (15)$$

According to Eq. (15), if T_Z , α , and β are given, all components of p ($p = [p_X \ p_Y \ p_Z]^T$) can be determined. Thus, r_k , which represents the displacement of Ni–Ti rods, can be obtained according to the geometry of the mechanism:

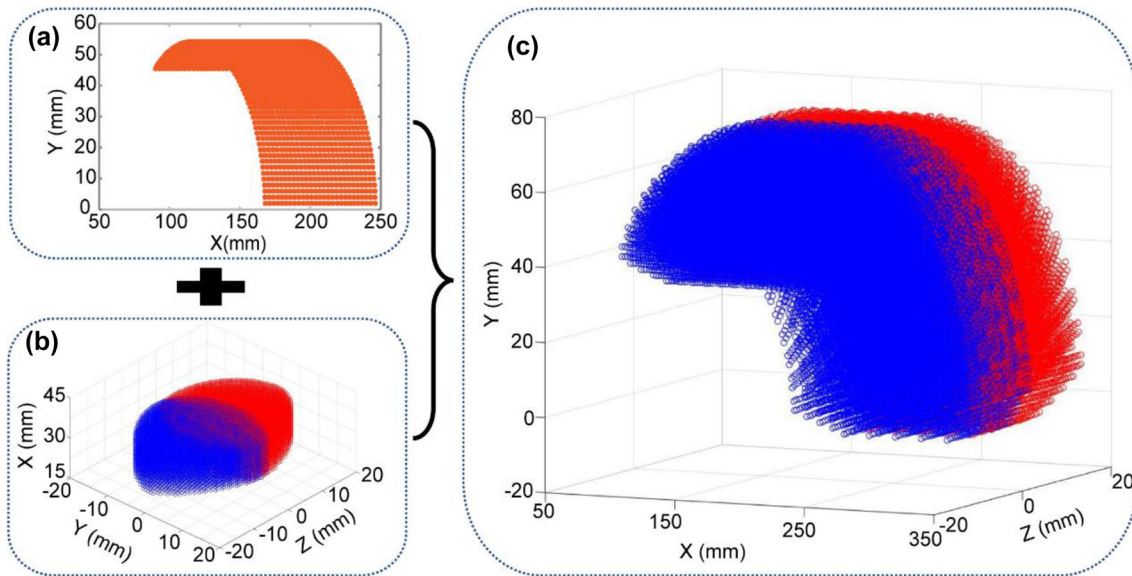


FIGURE 5. Simulation result of the workspace analysis. (a) Workspace of the guidance part. (b) Work space of the manipulator. (c) Workspace of the robot.

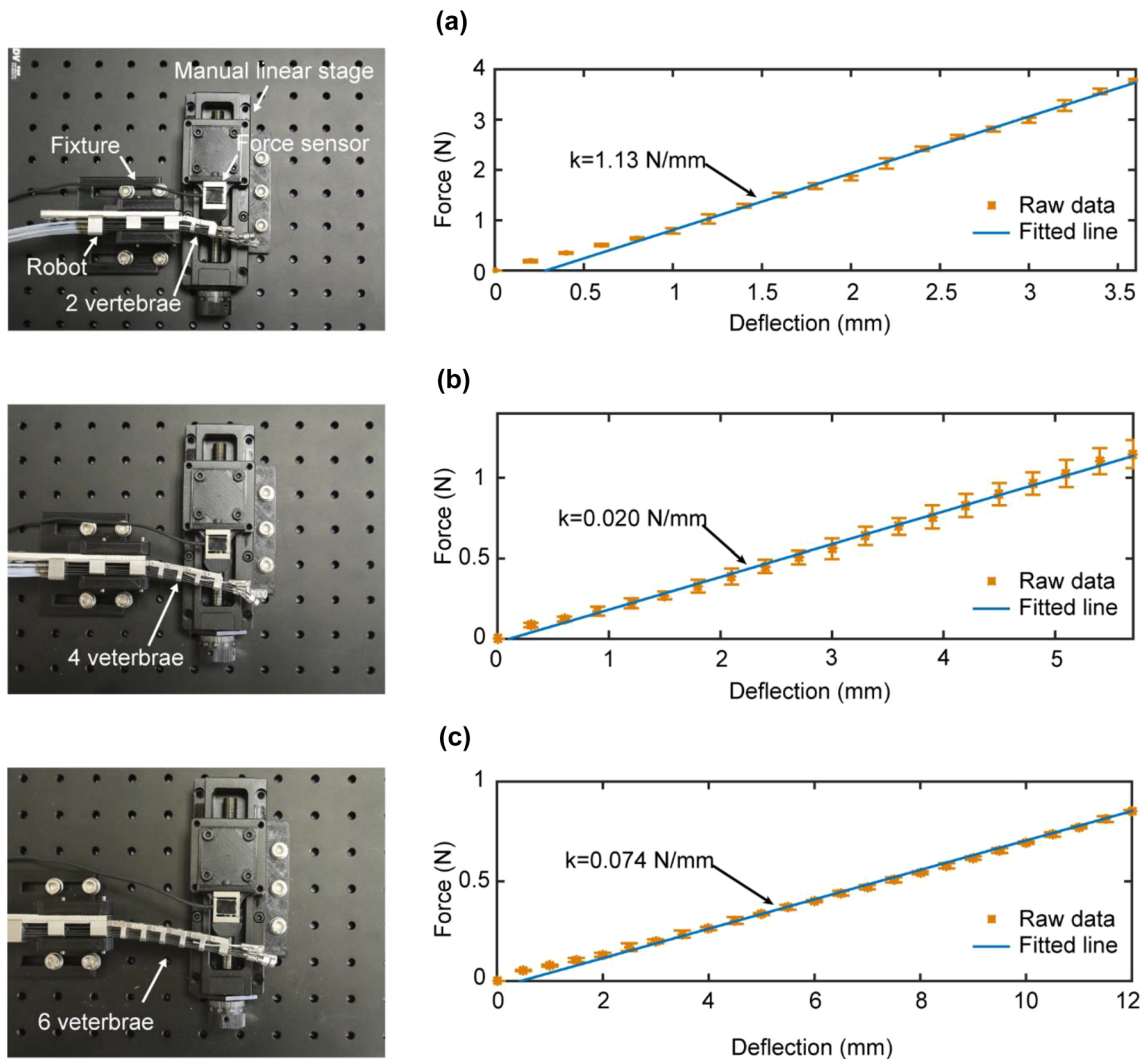


FIGURE 6. Bending stiffness test of the bendable segment with different numbers of vertebrae. (a) 2 Vertebrae. Left: experimental setup. Right: experimental results. (b) 4 Vertebrae. Left: experimental setup. Right: experimental results. (c) 6 Vertebrae. Left: experimental setup. Right: experimental results.

$$r_k = S_{kz} - \sqrt{s_k^2 - (S_{kX} - P_{kX})^2 - (S_{kY} - P_{kY})^2}. \quad (16)$$

Workspace Analysis

The reachable workspace of a robot is referred to as the set of positions that its distal end can access to, which serves as an important criterion for evaluating the kinematic performance of a robot and can be obtained by traversing all the variates of the configuration parameters within their limits with a certain step in MATLAB.¹⁷ Tables 2 and 3 present values of the configuration parameter of the guidance part and the manipulator, respectively, for workspace analysis.

Figure 5a illustrates the workspace of the guidance part. The guidance part can access most target points within the workspace at different bending angles, effectively enhancing flexibility and dexterity of the system. Figure 5b shows the workspace of two manipulators relative to the distal vertebra, which covers an area of 40 mm × 20 mm × 20 mm. The overlapped area of 10 mm × 20 mm × 20 mm indicates the ability of two manipulators to complete bimanual manipulations, which will not cause any damage to the manipulator due to the enhanced compliance resulting from the optimized parallel mechanism. The workspace of the designed robot is demonstrated in Fig. 3c, which is the combination of the workspaces of the guidance part and two manip-

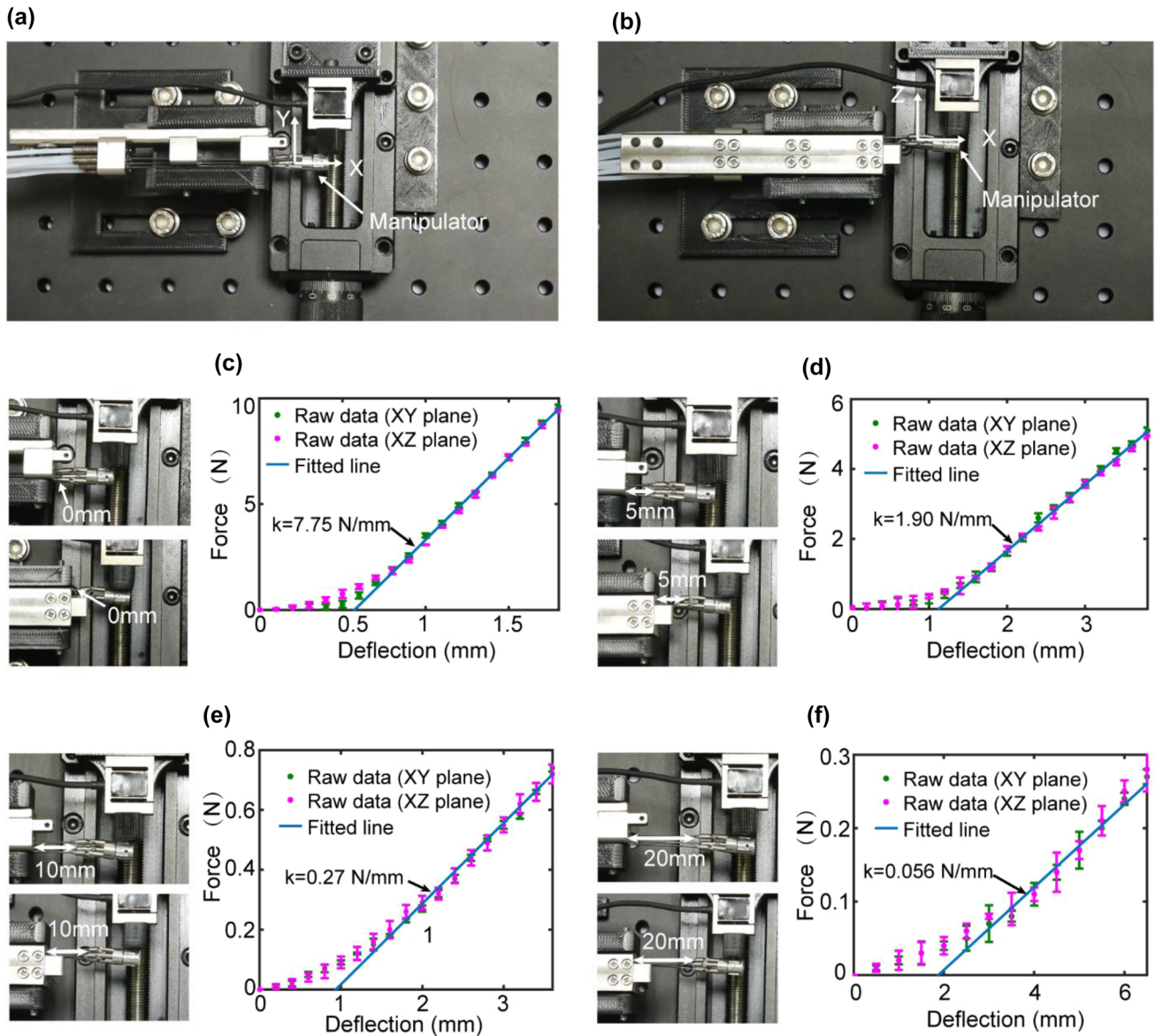


FIGURE 7. Bending stiffness test of the manipulator in different conditions. (a) Experimental setup for the test of the bending stiffness of the manipulator in the XY plane. (b) Experimental setup for the test of the bending stiffness of the manipulator in the XZ plane. (c) Displacement 0 mm. Top left: XY plane. Bottom left: XZ plane. Right: experimental results. (d) Displacement 5 mm. Top left: XY plane. Bottom left: XZ plane. Right: experimental results. (e) Displacement 10 mm. Top left: XY plane. Bottom left: XZ plane. Right: experimental results. (f) Displacement 20 mm. Top left: XY plane. Bottom left: XZ plane. Right: experimental results.

ulators. This arc-like area is markedly larger than the design goal.

Experimental Evaluation

As one of the most important characteristics, the bending stiffness determines the compliance of a robot, which was defined as the ratio of the applied force to the deflection generated in this experiment. Figures 6 and 7 illustrate the experimental setup for the bending stiffness analysis of the robot. As shown in the figure, a force sensor (JLBS-MD-1KG, Bengbu Sensor System

Engineering Co., Ltd., Anhui, China) was mounted to the slide block of a manual linear stage (PT48-75G, PDV Instrument Co., Ltd., Beijing, China). Both the robot and the linear stage were fixed to a solid aluminum optical breadboard (PT-02PB300×300, PDV Instrument Co., Ltd., Beijing, China), with the direction of the applied force in line with that of the deflection of the experiment object. In the experiment, the force sensor was moved by the linear stage with a fixed step to force the object to produce a deflection. Values of the deflection and the applied force were recorded to obtain the bending stiffness. The bending

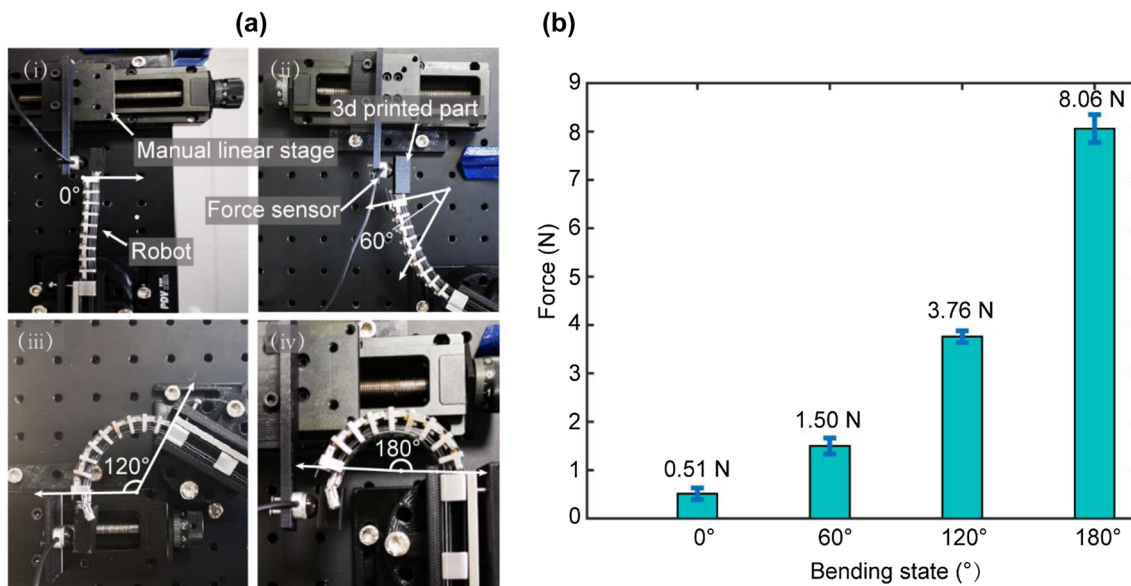


FIGURE 8. Load capability test of the robot. (a) Experimental setup. (i) 0°, (ii) 60°, (iii) 120°, and (iv) 180°. (b) Experimental results.

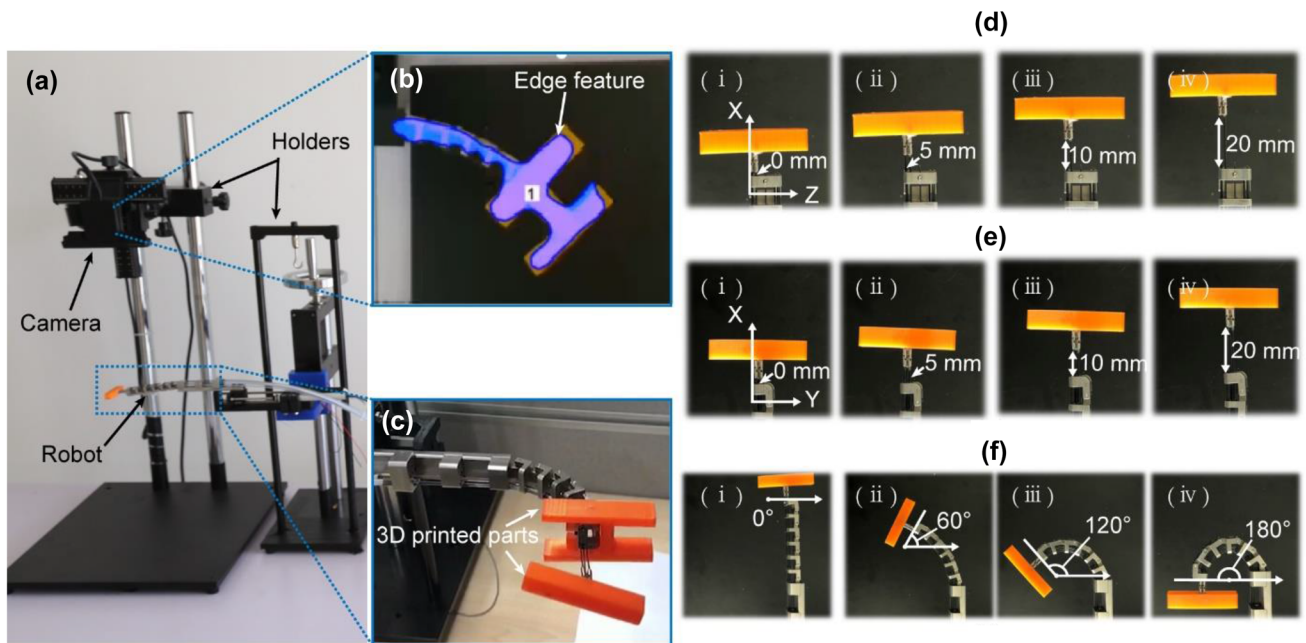


FIGURE 9. Positioning accuracy test of the robot. (a) Experimental setup. (b) Extracted edge feature of the robot. (c) Robot with enlarged widths. (d) Positioning accuracy test of the manipulator with different displacements in the XZ plane: (i) 0 mm, (ii) 5 mm, (iii) 10 mm, and (iv) 20 mm. (e) Positioning accuracy test of the manipulator with different displacements in the XY plane: (i) 0 mm, (ii) 5 mm, (iii) 10 mm, and (iv) 20 mm. (f) Positioning accuracy test of the manipulator when the bendable segment at different bending angles: (i) 0°, (ii) 60°, (iii) 120°, and (iv) 180°.

stiffness of the bendable segment was characterized for different numbers of vertebrae (2, 4, and 6) of the bendable segment, as depicted in Fig. 6. Additionally, the bending stiffness of the manipulator was characterized for different displacements of the manipulator (0, 5, 10, and 20 mm) for at different motioning planes

(XY plane and XZ plane), as shown in Fig. 7. To improve the reliability of the results, six sets of data were obtained and analyzed for each case.

In addition to improved compliance, the robot should have an adequate load capability to enable manipulation tasks, which was quantified and analyzed

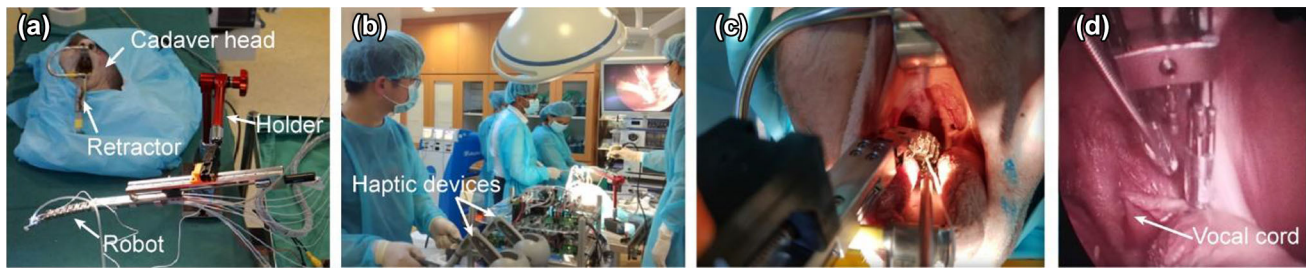


FIGURE 10. Cadaver trial. (a) Slave side of the surgical robotic system. (b) Master side. (c) Snapshot of the cadaver trial. (d) Endoscopic view of the robot in the target area.

in this work. As illustrated in Fig. 8, the experimental setup was similar to that of the bending stiffness test. A force sensor (OMD-10-SE-10N, OnRobot Corp, Odense, Denmark) was moved by a manual linear stage to contact and force the manipulator to generate a deflection when the bendable segment was in different bending states (0° , 60° , 120° , and 180°). A 3D-printed part was fixed to the manipulator to increase the contact area. Because the load capability of a robot is determined by its weakest component, the applied force was directed along the bending direction of the bendable segment. For surgical robots controlled in a master-slave mode, small deflections of less than 10% of the total length of the continuum structure, can be corrected by user inputs under an endoscopic view.^{13,34} The total length of the bendable segment is 86 mm. Therefore, the force required to push the manipulator to generate a deflection equal to 8 mm was obtained and utilized to evaluate the load capability of the robot. Each case was tested eight times to improve the reliability of the results.

The positioning accuracy of this surgical robotic system was analyzed using an optimized image-based motion detection method. Figure 9a illustrates the experimental setup of the positioning accuracy test of both the guidance part and the manipulator. A depth-sensing camera (SR300, Intel Corp, CA, USA) was utilized to capture the motion of the robot. The camera was mounted to holders and adjusted to ensure that the motion of the robot was consistently within the range of the camera. To overcome the shortcoming of conventional blob detection algorithms in extracting edge features of objects and to improve the detection accuracy, a polygonal approximation algorithm based on the Fourier descriptor was integrated into the blob detection technology.²⁹ Moreover, as shown in Fig. 9c, two 3D-printed parts with extended widths, were attached to the distal vertebra and the manipulator to eliminate the distortion resulting from the small size of the object and further improved the tracking precision. As demonstrated in Fig. 9b, the edge feature of the robot could be accurately extracted and recorded by the camera. To test the positioning accuracy of the

linear motion generated by the guidance part, only the guidance part was programmed to move forward at a speed of 1 mm/s. To study the positioning accuracy of the bending motion generated by the guidance part, the robot was driven to bend to 180° at a constant speed in two cases: (1) no compensation: only the bendable segment was programmed to bend. (2) With compensation: the manipulator was controlled to follow the bending motion of the bendable segment at the same speed. The trajectories of both the distal vertebra and the manipulator were recorded and are plotted in Fig. 11a. To investigate the effects of various possible factors, such as the simplification of the kinematic model, the stiffness characteristic, and different bending directions, on the positioning accuracy, the manipulator was programmed to bend to 45° at a constant speed of $3^\circ/\text{s}$ under different conditions, including different displacements (0, 5, 10, 20 mm) and different motion planes (XZ plane and YZ plane), as demonstrated in Figs. 9d and 9e. In addition, the impact induced by the interference between different mechanisms on the positioning accuracy of the manipulator was studied by controlling the manipulator to move forward or bend at constant speeds, when the bendable segment was positioned at different bending angles (0° , 60° , 120° , and 180°), as shown in Fig. 9f. The trajectory and positioning error of the manipulator in different conditions are plotted in Figs. 11b and 11c, respectively.

To further demonstrate the feasibility and advantages of the developed surgical robotic system in TORS, a cadaver trial was carried out. For robotic surgery, the initial setup is necessary before the first-time operation of a robotic system or after the replacement of the surgical instrument, which will be repeated several times in a procedure. Consequently, the setup time is one of the key factors influencing the operative time, which becomes an important index to evaluate the performance of a surgical robotic system.^{1,18} The initial setup of the developed surgical robotic system included the following steps. First, the sterilized robot was mounted to a 7-DOF magnetic-based holder. Then, the robot was moved to approach

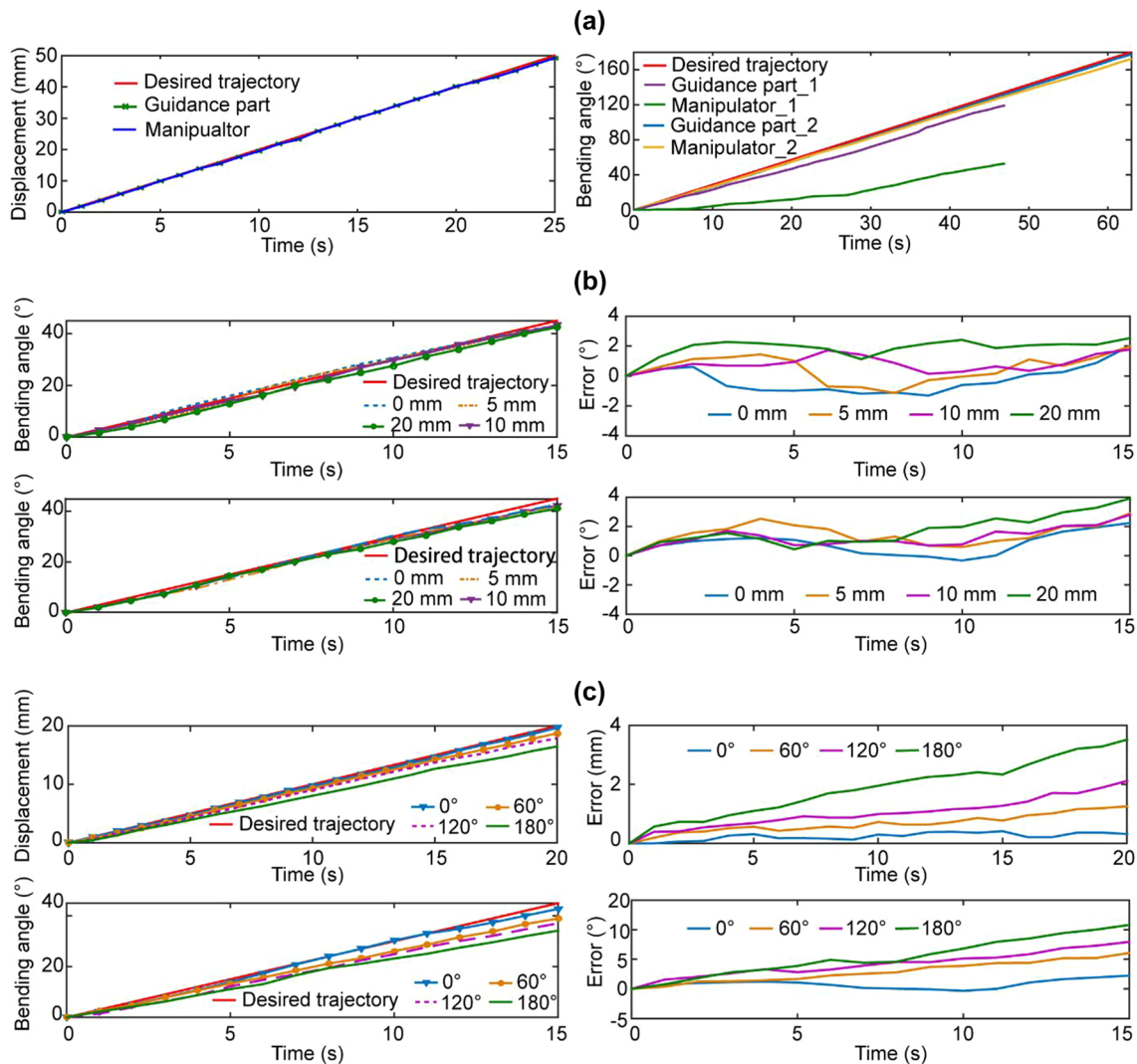


FIGURE 11. Experimental results of the positioning accuracy test of the robot. (a) Motion trajectory of the guidance part and the manipulator. Left: linear motion. Right: bending motion. (b) Experimental results of the manipulator with different displacements. Top left: trajectory of the bending motion in the XY plane. Top right: position error of the bending motion in the XY plane. Bottom left: trajectory of the bending motion in the XZ plane. Bottom right: position error of the bending motion in the XZ plane. (c) Experimental results of the manipulator when the bendable segment at different bending angles. Top left: trajectory of the linear motion. Top right: position error of the linear motion. Bottom left: trajectory of the bending motion. Bottom right: position error of the bending motion.

the cadaver head, whose mouth was kept open by a retractor, as illustrated in Fig. 10a, with the distal part located in the front part of its oral cavity. The tilt angle of the robot was then adjusted to approximately 80° to ensure that the distal end faced the throat. Finally, the robotic system was powered on to complete the operation. The time to complete these steps was recorded, which was repeated by five different people who participated in the cadaver. Similarly to most surgical robotic systems, the system developed in this work was also controlled in a master–slave teleoperation mode. After the initial setup, the operator could manipulate

two haptic devices (Phantom Omni, Geomagic, Inc., North Carolina, USA) on the master side to steer the guidance part of the robot to transversally reach the target surgical site, as illustrated in Fig. 10b. The time required for the robot to access the surgical site is another critical criterion determining the operative time, which was measured in this cadaver trial. Three people, who participated in the cadaver trial but had never operated this surgical robotic system, were trained to complete the experiment. After becoming familiar with the operation of this system, they were asked to steer the robot to access the vocal cord. The

times required for the robot to reach the target site, which was steered by different operators, was recorded.

RESULTS

Bending Stiffness Characterization

Figures 6 and 7 show the experimental results pertaining to the bending stiffness characterization of both the bendable segment and the manipulator, all of which present a similar variation tendency. Except for those at the beginning stage, the mean values of the experimental data can be well fitted by straight lines with the coefficients of determination R^2 greater than 0.997, whose gradient can be regarded as the bending stiffness. The nonlinearity of the beginning state resulted from the gap between Ni–Ti rods and pinholes in the vertebra of the bendable segment, which only occurred when the deflection was quite small and had a limited influence on the bending stiffness of the robot. For the bendable segment, the bending stiffness decreased remarkably with the increase in the number of vertebrae, contributing to improved compliance and safer robot-tissue interactions. In this design, 6 vertebrae are utilized to constitute the bendable segment. More vertebrae will lead to an insufficient load capability. The bending stiffness of the manipulator is irrelevant to the bending directions but determined by the displacement. Larger displacement results in a smaller bending stiffness of the manipulator. The quantitative relationship between the displacement and the bending stiffness of the manipulator will be investigated in our future work.

Load Capability Evaluation

The experimental results of the load capability test are shown in Fig. 8b. When the same deflection is generated, a large force indicates a high load capability. Thus, the robot achieves increased load capability when the bending angle of the bendable segment increases. In practice, the common bending range of this robot is from 60° to 120° , within which the load capability of the robot is greater than 1.5 N.

Positioning Accuracy Test

Figure 11a illustrates the trajectory of the guidance part and the manipulator under predefined conditions. Experimental results suggest that the guidance part achieves a high positioning accuracy in its linear motion. Additionally, the linear motion of the guidance

part has no influence on the manipulator. Nevertheless, significant errors between the experimental results (the purple solid line denotes the trajectory of the bendable segment and the green solid line represents the trajectory of the manipulator) and the desired trajectory (the red solid line) of the bending motion can be observed if no compensation is made. As plotted in Fig. 11a, the guidance part became stuck at an angle of approximately 120° when the manipulator was driven to its limit bending angle of approximately 50° . The interaction force, which drove the bending motion of the manipulator, served as the external load for the bendable segment, resulting in the invalidation of the kinematic model of the guidance part and leads to the degradation of the positioning accuracy. This problem could be effectively alleviated by the proposed compensation method, with which both the bendable segment (the blue solid line) and manipulator (the yellow solid line) were able to follow the desired trajectory with a significantly improved accuracy.

As shown in Fig. 11b, the manipulator achieves similar positioning accuracy in different planes or at different displacements, confirming that the bending direction and the variable stiffness characteristic of the manipulator have little effect on the positioning accuracy of the manipulator. Furthermore, the maximum positioning errors of all cases are all smaller than 4° , which is less than 9% of the maximum motion range and indicates that the manipulator achieves acceptable positioning accuracy with the derived kinematic model. Machining and assembly errors are considered the main reason for these positioning errors, which can be reduced in future versions.

As illustrated in Fig. 11c, the manipulator is able to achieve a relatively high positioning accuracy in both the linear motion and the bending motion when the bendable segment is in its initial state, which significantly increases with the bending angle of the bendable segment. The friction is regarded as the main cause of this result, whose magnitude is positively associated with the bending angle of the bendable segment. The Ni–Ti rods are compelled to generate axial compression or extension to overcome this friction before driving the manipulator, decreasing the positioning accuracy.³³ Over the common bending range (60° to 120°), the maximum displacement error is approximately 2 mm and the maximum bending error is approximately 7.5° . Considering that this surgical robotic system is controlled in a master–slave teleoperation mode, these errors can be easily corrected by the operator's inputs. Consequently, the overall positioning accuracy of the manipulator is acceptable for TORS.

Cadaver Trial

In the cadaver trial, the average time for five participants to finish the initial setup was approximately 2 min (standard deviation 23 s), which satisfied the design goal. When the system was powered on, the developed surgical robot was well controlled in the master–slave mode. Moreover, the robot demonstrated adequate flexibility and compliance during the traversal of the oral cavity and when entering the larynx. As a result, no trauma was caused by the robot to the surrounding tissues. The average time for the robot to access the vocal cord, which was controlled by three beginners, was approximately 1 min and 30 s (standard deviation 42 s). Additionally, two manipulators were controlled to contact the vocal cord from different angles showing excellent dexterity.

DISCUSSION AND CONCLUSION

In this work, a flexible and compliant surgical robotic system was developed for TORS. The flexible parallel mechanism was optimized and integrated with the continuum robot for the first time in the development of a surgical robot to satisfy strict TORS requirements. The robot designed based on this hybrid mechanism retains all advantages, such as flexibility, dexterity, and simple structure, of the optimized flexible parallel mechanism while inheriting the compactness and compliance of the continuum robot. As a result, this design features an improved stability and higher load capability than does the interleaved continuum-rigid robot⁶ and a larger workspace when compared with that of the continuum parallel robot.³ Ample analysis and experiments were conducted to evaluate the performance of the designed surgical robot. As indicated by the simulation results, the workspace of the robot can cover the entire target area. In addition, experimental results of the bending stiffness characterization suggest that the designed robot can maintain good compliance in all cases, which contributes to the safe interaction with patient tissues. Moreover, the load capability of the robot is better than that of other designs employing Ni–Ti rods,^{13,35} which generated smaller deflections under the same payload, and satisfies the requirements of TORS.¹⁹ The positioning accuracy of the designed surgical robotic system in various conditions is verified to be acceptable for TORS, which can be further enhanced by improving the machining accuracy and eliminating the errors caused by the frictions using control algo-

rithms to complete more precise tasks. Moreover, the interference between the optimized flexible parallel mechanism and the continuum structure of the robot exerts limited influence on the positioning accuracy of the robot. To further prove the robot's feasibility in TORS, a cadaver trial was designed and conducted, whose results suggest that the size, flexibility, compliance, and workspace of the designed robot satisfy the requirements of TORS. Additionally, the setup time of this surgical robotic system is much shorter than those reported for current commercialized systems (da Vinci[®] robotic system: 30 min,¹ Flex[®] surgical system: 9 min¹⁸). The average time for the robot to access the surgical site in the larynx was less than half the time required by the Flex[®] surgical system to expose the endolarynx, which requires 3 min and 38 s.¹⁴ This time can be further reduced if the proficiency in manipulation is improved or more navigation technologies are engaged. The reduced setup time and the reduced time required to access the target surgical site contribute to the decreased operative time and improved operative efficiency, which is beneficial to both patients and doctors. In addition, these results imply that the developed surgical robotic system is easy to use for beginners.

This work aimed to provide the proof of concept. A number of limitations need to be overcome to further improve the performance of the developed surgical robotic system. The guidance part has two DOFs and is only capable of moving in a fixed plane. Due to the small size of the manipulator, existing surgical instruments are not applicable to this system. Additionally, there is a slight time delay between the master controller and the slave robot.

A tremendous amount of work remains to be done before the proposed robot can be employed in clinical applications. The motion of the guidance part will be extended from planar motion to three-dimensional movements. In addition, suitable control algorithms will be implemented to reduce the time delay between the master side and the slave side while retaining the stability of the system. To further increase the safety of the system, the robot part will be covered with specialized and sterilized wraps. Moreover, surgical instruments, which can be conveniently equipped to the manipulator and replaced by others, will be carefully designed. In addition to TORS, the feasibility of the developed robotic surgical system in other robotic-assisted MIS will also be investigated with more cadaver or animal experiments.

ELECTRONIC SUPPLEMENTARY MATERIAL

The online version of this article (doi:<https://doi.org/10.1007/s10439-019-02241-0>) contains supplementary material, which is available to authorized users.

ACKNOWLEDGMENTS

This work is supported by the Singapore NMRC Bedside and Bench under Grant R-397-000-245-511 and National Key Research and Development Program, The Ministry of Science and Technology (MOST) of China (No. 2018YFB1307703), both awarded to Dr. Hongliang Ren.

REFERENCES

- ¹Ayav, A., L. Bresler, L. Brunand, and P. Boissel. Early results of one-year robotic surgery using the Da Vinci system to perform advanced laparoscopic procedures. *J. Gastrointest. Surg.* 8:720–726, 2004.
- ²Bergeles, C., and G. Z. Yang. From passive tool holders to microsurgions: safer, smaller, smarter surgical robots. *IEEE Trans. Biomed. Eng.* 61:1565–1576, 2014.
- ³Black, C. B., J. Till, and D. C. Rucker. Parallel continuum robots: modeling, analysis, and actuation-based force sensing. *IEEE Trans. Robot.* 34:29–47, 2018.
- ⁴Burgner-Kahrs, J., D. C. Rucker, and H. Choset. Continuum robots for medical applications: a survey. *IEEE Trans. Robot.* 31:1261–1280, 2015.
- ⁵Chang, T., Y. Tian, C. Li, X. Gu, K. Li, H. Yang, P. Sanghani, C. Lim, H. Ren, and P. Y. Chen. Stretchable graphene pressure sensors with Shar-Pei-like hierarchical wrinkles for collision-aware surgical robotics. *ACS Appl. Mater. Interfaces* 2019. <https://doi.org/10.1021/acsami.9b00166>.
- ⁶Conrad, B. L., and M. R. Zinn. Interleaved continuum-rigid manipulation approach: development and functional evaluation of a clinical scale manipulator, pp. 4290–4296, 2014. <https://doi.org/10.1109/IROS.2014.6943168>.
- ⁷Daniel, M. M. L. M. Pharyngeal dimensions in healthy men and women. *Clinics* 62:5–10, 2007.
- ⁸Dogangil, G., B. L. Davies, F. Rodriguez, and Y. Baena. A review of medical robotics for minimally invasive soft tissue surgery. *Proc. Inst. Mech. Eng. H* 224:653–679, 2009.
- ⁹Guthart, G., and J. K. Salisbury Jr. The Intuitive™ telesurgery system: overview and application, 2000. <https://doi.org/10.1109/robot.2000.844121>.
- ¹⁰Ho, M., Y. Kim, S. S. Cheng, R. Gullapalli, and J. P. Desai. Design, development, and evaluation of an MRI-guided SMA spring-actuated neurosurgical robot. *Int. J. Robot. Res.* 34:1147–1163, 2015.
- ¹¹Hockstein, N. G., and B. W. O'Malley. Transoral robotic surgery. *Oper. Tech. Otolaryngol. Head Neck Surg.* 19:67–71, 2008.
- ¹²Hong, M. B., and Y. H. Jo. Design of a novel 4-DOF wrist-type surgical instrument with enhanced rigidity and dexterity. *IEEE/ASME Trans. Mechatron.* 19:500–511, 2014.
- ¹³Hong, W., L. Xie, J. Liu, Y. Sun, K. Li, and H. Wang. Development of a novel continuum robotic system for maxillary sinus surgery. *IEEE/ASME Trans. Mechatron.* 23:1226–1237, 2018.
- ¹⁴Johnson, P. J., C. R. Serrano, M. Castro, R. Kuenzler, and H. Choset. Demonstration of transoral surgery in cadaveric specimens with the medrobotics flex system. *Laryngoscope* 2013. <https://doi.org/10.1002/lary.23512>.
- ¹⁵Li, C., X. Gu, X. Xiao, C. M. Lim, and H. Ren. A robotic system with multi-channel flexible parallel manipulators for single port access surgery. *IEEE Trans. Ind. Inform.* 2018. <https://doi.org/10.1109/TII.2018.2856108>.
- ¹⁶Li, Z., and C. S. H. Ng. Future of uniportal video-assisted thoracoscopic surgery—emerging technology. *Ann. Cardiothorac. Surg.* 5:127–132, 2016.
- ¹⁷Li, Z., L. Wu, H. Ren, and H. Yu. Kinematic comparison of surgical tendon-driven manipulators and concentric tube manipulators. *Mech. Mach. Theory* 107:148–165, 2017.
- ¹⁸Mandapathil, M., B. Greene, and T. Wilhelm. Transoral surgery using a novel single-port flexible endoscope system. *Eur. Arch. Otorhinolaryngol.* 2015. <https://doi.org/10.1007/s00405-014-3177-1>.
- ¹⁹Nadeau, C., H. Ren, A. Krupa, and P. E. Dupont. Intensity-based visual servoing for instrument and tissue tracking in 3D ultrasound volumes. *IEEE Trans. Autom. Sci. Eng.* 12:367–371, 2015.
- ²⁰Park, Y. M., W. S. Kim, H. K. Byeon, S. Y. Lee, and S. Kim. Oncological and functional outcomes of transoral robotic surgery for oropharyngeal cancer. *Br. J. Oral Maxillofac. Surg.* 51:408–412, 2013.
- ²¹Phee, S. J., S. C. Low, V. A. Huynh, A. P. Kencana, Z. L. Sun, and K. Yang. Master and slave transluminal endoscopic robot (MASTER) for natural orifice transluminal endoscopic surgery (NOTES). *Conf. Proc. IEEE Eng. Med. Biol. Soc.* 2009:1192–1195, 2009.
- ²²Poon, H., C. Li, W. Gao, H. Ren, and C. M. Lim. Evolution of robotic systems for transoral head and neck surgery. *Oral Oncol.* 87:82–88, 2018.
- ²³Reboulet, C., and S. Durand-Leguay. Optimal design of redundant parallel mechanism for endoscopic surgery, pp. 1432–1437, 1999. <https://doi.org/10.1109/IROS.1999.811680>.
- ²⁴Ren, H., C. M. Lim, J. Wang, W. Liu, S. Song, Z. Li, G. Herbert, Z. T. H. Tse, and Z. Tan. Computer-assisted transoral surgery with flexible robotics and navigation technologies: a review of recent progress and research challenges. *Crit. Rev. Biomed. Eng.* 41:365–391, 2013.
- ²⁵Rivera-Serrano, C. M., P. Johnson, B. Zubiate, R. Kuenzler, H. Choset, M. Zenati, S. Tully, and U. Duvvuri. A transoral highly flexible robot. *Laryngoscope* 122:1067–1071, 2012.
- ²⁶Rock, J. P. T. F. Transoral surgery: an anatomic study. *Skull Base Surg.* 3:109, 1993.
- ²⁷Rose, A., C. Wohlleber, S. Kassner, H. F. Schlaak, and R. Werthschützky. A novel piezoelectric driven laparoscopic instrument with multiple degree of freedom parallel kinematic structure, pp. 2162–2167, 2009. <https://doi.org/10.1109/IROS.2009.5354507>.
- ²⁸Shang, J., C. J. Payne, J. Clark, D. P. Noonan, and K. W. Kwok. Design of a multitasking robotic platform with flexible arms and articulated head for minimally invasive surgery, pp. 1988–1993, 2012. <https://doi.org/10.1109/iros.2012.6385567>.
- ²⁹Smisek, J. P. T. 3D Camera Calibration. MSc Thesis, 2011.

- ³⁰Taylor, R. H., and D. Stoianovici. Medical robotics in computer-integrated surgery. *IEEE Trans. Robot. Autom.* 2016. <https://doi.org/10.1109/TRA.2003.817058>.
- ³¹Vitiello, V., S. L. Lee, T. P. Cundy, and G. Z. Yang. Emerging robotic platforms for minimally invasive surgery. *IEEE Rev. Biomed. Eng.* 6:111–126, 2013.
- ³²Wu, L., X. Yang, K. Chen, and H. Ren. A minimal POE-based model for robotic kinematic calibration with only position measurements. *IEEE Trans. Autom. Sci. Eng.* 12:758–763, 2015.
- ³³Xu, K., and N. Simaan. Actuation compensation for flexible surgical snake-like robots with redundant remote actuation, pp. 4148–4154, 2006. <https://doi.org/10.1109/robot.2006.1642340>.
- ³⁴Xu, K., R. E. Goldman, J. Ding, P. K. Allen, D. L. Fowler, and N. Simaan. System design of an insertable robotic effector platform for single port access (SPA) surgery, pp. 5546–5552, 2009. <https://doi.org/10.1109/iros.2009.5354028>.
- ³⁵Xu, K., J. Zhao, and M. Fu. Development of the SJTU unfoldable robotic system (SURS) for single port laparoscopy. *IEEE/ASME Trans. Mechatron.* 20:2133–2145, 2015.

Publisher's Note Springer Nature remains neutral with regard to jurisdictional claims in published maps and institutional affiliations.